Journal of Sound and Vibration (2001) **240**(1), 1–18
doi:10.1006/jsvi.2000.3202, available online at http://www.idealibrary.com on IDEAL®

DYNAMIC BEHAVIOUR OF A LAYER OF DISCRETE PARTICLES, PART 1: ANALYSIS OF BODY WAVES AND EIGENMODES

A. S. J. Suiker

Delft University of Technology, Koiter Institute Delft/Faculty of Aerospace Engineering, P.O. Box 5058, 2600 *GB Delft, The Netherlands. E-mail: a.suiker@lr.tudelft.nl*

A. V. Metrikine

Delft University of Technology, Faculty of Civil Engineering and Geosciences, P.O. Box 5048, 2600 *GA Delft, The Netherlands*

AND

R. De Borst

Delft University of Technology, Koiter Institute Delft/Faculty of Aerospace Engineering, P.O. Box 5058, 2600 *GB Delft, The Netherlands*

(*Received* 27 *January* 2000, *and in final form* 31 *May* 2000)

This paper is one in a series of two, and discusses the body wave propagation and the eigenmodes for a layer of discrete particles. This configuration is a representation for a ballast layer used in ordinary railway tracks. The discrete nature of the ballast is simulated via an elastic nine-cell square lattice. After deriving the equations of motion for the lattice, the long-wave approximation for the equations of motion is compared with the equations of motion for a classic elastic continuum. This comparison yields relations between the macroscopic continuum parameters and the microscopic lattice parameters. Then, the dispersion curves that characterize the eigenmodes of the discrete layer are derived. The differences between these dispersion curves and those of a continuous layer are elucidated. By means of a parametric study, the influence is shown of the particle diameter and thickness of the layer on the dynamic response. In an accompanying paper, the layer response to a moving, harmonically vibrating load is analyzed, which is a representation for a ballast track that is subjected to an instantaneous train axle passage.

1. INTRODUCTION

In the development of the high-speed railway lines, analysis of the structural wave processes generated by the train is necessary for a proper assessment of the deterioration and safety aspects of a railway system. An important wave type in such analyses is the surface wave, which, by definition, carries its energy along the surface of the track structure. The group velocity of a surface wave may be of the same magnitude as that of the train velocity. The ensuing accumulation of the energy under the train wheels can be characterized as *resonance*, resulting in a considerable amplification of the train–track response. The train velocities at which this occurs are commonly named *critical velocities* (see, for example, references [1, 2]). Track measurements in England [3] and in France [4] as well as visual

0022-460X/01/060001 + 18 $35.00/0

track inspections in these and other countries have revealed the *in situ* existence of critical train velocities. Consequently, for safety reasons and to limit track deterioration, train speed limits have been imposed on currently operating high-speed railway lines.

The magnitude of the critical velocities generally depends on the geometry and material characteristics of the railway track. For a ballast layer on a softer substratum of sand, clay or peat, various moving load models [1, 2, 5], as well as *in situ* track measurements [3] have shown that the lowest critical velocity occurs at/near the Rayleigh wave velocity of the soft substratum. Indeed, for this configuration the dynamic response is mainly characterized by the substratum properties. On the contrary, when a ballast layer is supported by a stiffer substratum of concrete (railway foundations, bridges or tunnels) or rock, the ballast layer itself is the determining factor in the characterization of the structural response. This is especially the case when the train vehicle induces strong vibrations, as for example, generated by the sleeper distance [6–9]. The emphatic influence of the ballast properties on the structural response is due to multiple reflections of the train-induced waves at the ballast–substratum interface, causing the wave energy to be captured within the ballast layer. Correspondingly, the ballast layer behaves as a waveguide.

Although the studies mentioned above have explained important features of high-speed railway systems, it has to be realized that the models used in these studies are constructed within a continuum mechanics framework. As the nature of the continuum mechanics theory results in a limited accuracy level with regard to the modelling of heterogeneous effects by the discrete particles, the representation by these models becomes less accurate when the transmitted wavelength reaches the order of magnitude of the ballast particle size. The analysis of such heterogeneous effects is most relevant in the case of a ballast layer on a stiffer substratum, since then the ballast layer is able to guide waves with a relatively short wavelength.

For a better understanding of the particle interactions in a ballasted railway track, the dynamic response of a rigidly supported layer of discrete particles is analyzed in a series of two papers. In this paper, the body wave propagation through the discrete layer is examined, as well as the dispersion branches that reflect the eigenmodes of the layer. In the companion paper, the steady state response of the layer to a moving, harmonically vibrating load will be elaborated. Here, the moving load is supposed to represent an instantaneous train axle passage. The discrete layer is modelled by a square lattice consisting of individual cells that are mutually connected via elastic longitudinal springs and shear springs. The distance between the cells thus equals the ballast particle size. It is justified to use an elastic material law for the lattice, since the response of a ballast layer to an instantaneous train axle passage is mainly reversible. Although a railway structure is a typical three-dimensional structure, the ballast layer has been modelled in a two-dimensional manner. Nevertheless, the plane in which the load propagates strongly determines the characteristics of the dynamic response, so that, apart from the different geometrical radiation, the dynamic characteristics of two-dimensional moving load models and three-dimensional moving load models are equivalent [2].

After deriving the equations of motion for an inner cell (i.e., a cell in the interior of the layer) and a boundary cell (i.e., a cell at the surface of the layer), the long-wave approximation of the lattice wave equations is compared with the wave equations of the classic elastic continuum (see also, references [10–12]). This comparison results in a relation between the macroscopic constitutive parameters of the continuum model and the microscopic constitutive parameters of the discrete lattice model. Then, the propagation characteristics of the body waves in the lattice are derived, followed by the derivation of the dispersion curves that reflect the eigenmodes of the discrete layer. These dispersion curves

are compared to those of a correspondent elastic continuous layer, where the typical features of the particle diameter and the layer thickness are illustrated via a parametric study.

2. THE GOVERNING EQUATIONS FOR A SQUARE LATTICE

In Figure 1, a rigidly supported layer of equal-sized, circular particles with diameter d is depicted. This configuration represents a ballast layer of a common railway track. Trivially, the assumption of all particles having the same size is a simplification of an *in situ* ballast gradation. The internal layer geometry as well as the micro-structural particle interactions are modelled by a square lattice. The square lattice consists of individual cells that are connected to each other via elastic longitudinal springs and shear springs. Here, two different cell types can be distinguished, which are the *inner cell* situated in the interior of the layer and the *boundary cell* situated at the free surface of the layer. In this section, for both cell types the equations of motion are derived, where it is required that in the long-wave limit the equations of motion for the inner cell reduce to those of the standard elastic continuum.

2.1. EQUATIONS OF MOTION FOR AN INNER CELL

Figure 2 shows an inner cell in the interior of the square lattice. The inner cell has dimensionless co-ordinates (m, n), and is connected via axial longitudinal springs K^n_{axi} and axial shear springs K^s_{axi} to four neighbouring mid-side cells at distance d, and via diagonal longitudinal springs K^n_{dia} and diagonal shear springs K^s_{dia} to four neighbouring edge cells at distance $\sqrt{2}d$. The lattice cells have two degrees of freedom, which are the displacements in x and z directions $\{u_x, u_z\}$. The dynamic behaviour of the inner cell (m, n) can be expressed in terms of the Lagrangian L, according to

$$L^{(m,n)} = E^{(m,n)}_{kin} - E^{(m,n)}_{pot}, \tag{1}$$

with E_{pot} the potential energy and E_{kin} the kinetic energy. The potential energy may be formulated as

$$E^{(m,n)}_{pot} = \tfrac{1}{2}\sum_{i=1}^{4} (\Delta l^2_{(i)} K^n_{axi} + \Delta s^2_{(i)} K^s_{axi}) + \tfrac{1}{2}\sum_{i=5}^{8} (\Delta l^2_{(i)} K^n_{dia} + \Delta s^2_{(i)} K^s_{dia}), \tag{2}$$

in which $\Delta l_{(i)}$ and $\Delta s_{(i)}$ are the length variations of the ith spring in the longitudinal direction and in the shear direction. In correspondence with Figure 2, the linear form of these length

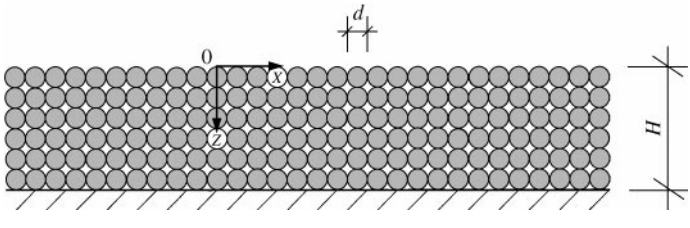

Figure 1. Layer of equal-sized, circular particles.

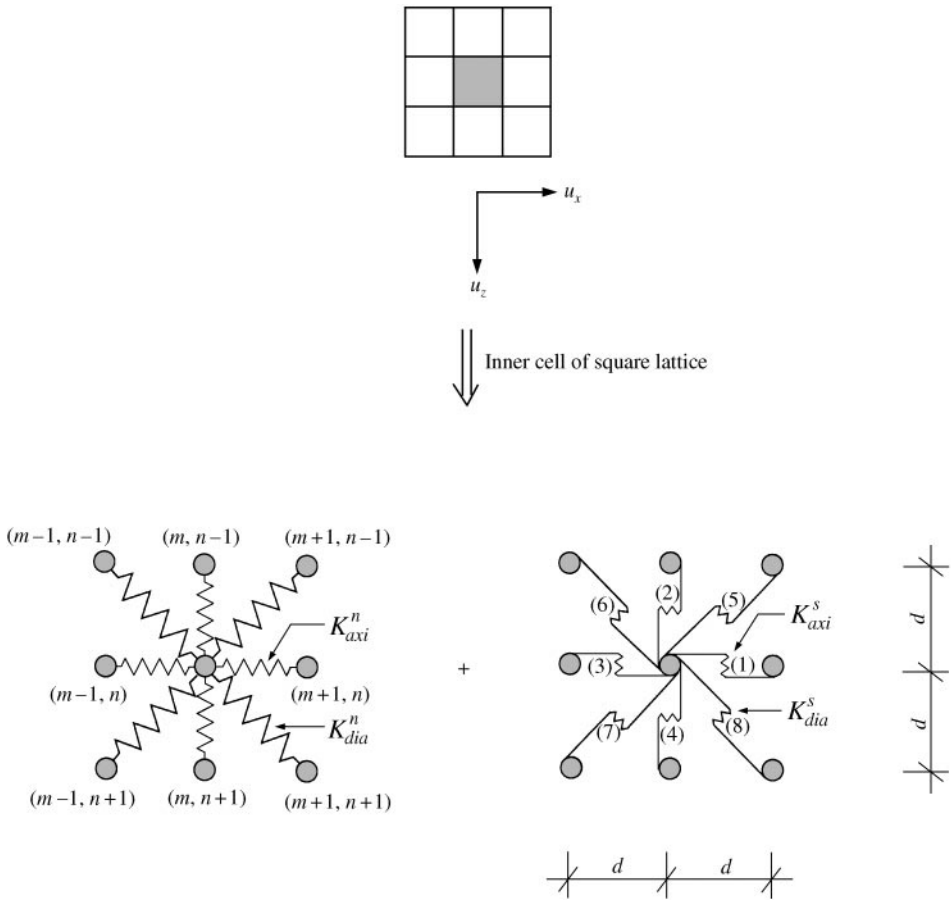

Figure 2. Inner cell of square lattice.

variations is as follows:

$$\Delta l_{(1)} = u_x^{(m+1,n)} - u_x^{(m,n)}, \quad \Delta l_{(2)} = u_z^{(m,n)} - u_z^{(m,n-1)},$$

$$\Delta l_{(3)} = u_x^{(m,n)} - u_x^{(m-1,n)}, \quad \Delta l_{(4)} = u_z^{(m,n+1)} - u_z^{(m,n)},$$

$$\Delta l_{(5)} = \tfrac{1}{2}\sqrt{2}\,(u_z^{(m,n)} - u_z^{(m+1,n-1)} - u_x^{(m,n)} + u_x^{(m+1,n-1)}),$$

$$\Delta l_{(6)} = \tfrac{1}{2}\sqrt{2}\,(u_z^{(m,n)} - u_z^{(m-1,n-1)} - u_x^{(m-1,n-1)} + u_x^{(m,n)}),$$

$$\Delta l_{(7)} = \tfrac{1}{2}\sqrt{2}\,(u_z^{(m-1,n+1)} - u_z^{(m,n)} - u_x^{(m-1,n+1)} + u_x^{(m,n)}),$$

$$\Delta l_{(8)} = \tfrac{1}{2}\sqrt{2}\,(u_z^{(m+1,n+1)} - u_z^{(m,n)} - u_x^{(m,n)} + u_x^{(m+1,n+1)}),$$

$$\Delta s_{(1)} = u_z^{(m+1,n)} - u_z^{(m,n)}, \quad \Delta s_{(2)} = u_x^{(m,n-1)} - u_x^{(m,n)},$$

$$\Delta s_{(3)} = u_z^{(m,n)} - u_z^{(m-1,n)}, \quad \Delta s_{(4)} = u_x^{(m,n)} - u_x^{(m,n+1)},$$

$$\Delta s_{(5)} = \tfrac{1}{2}\sqrt{2}\,(u_z^{(m+1,n-1)} - u_z^{(m,n)} - u_x^{(m,n)} + u_x^{(m+1,n-1)}),$$

$$\Delta s_{(6)} = \tfrac{1}{2}\sqrt{2}\,(u_z^{(m,n)} - u_z^{(m-1,n-1)} - u_x^{(m,n)} + u_x^{(m-1,n-1)}),$$

$$\Delta s_{(7)} = \tfrac{1}{2}\sqrt{2}\,(u_z^{(m,n)} - u_z^{(m-1,n+1)} - u_x^{(m-1,n+1)} + u_x^{(m,n)}),$$

$$\Delta s_{(8)} = \tfrac{1}{2}\sqrt{2}\,(u_z^{(m+1,n+1)} - u_z^{(m,n)} - u_x^{(m+1,n+1)} + u_x^{(m,n)}). \tag{3}$$

Additionally, the kinetic energy of the inner cell (m, n) is given by

$$E_{kin}^{(m,n)} = \tfrac{1}{2}M[(\dot{u}_x^{(m,n)})^2 + (\dot{u}_z^{(m,n)})^2], \tag{4}$$

in which M represents the cell mass. The superimposed dot designates the full derivative with respect of time, so that $\{\dot{u}_x^{(m,n)}, \dot{u}_z^{(m,n)}\}$ represent the velocities in x and z directions respectively. Combining expressions (1)–(4), followed by applying the Lagrange equations (see, for example, reference [13]), yields

$$\frac{\partial L^{(m,n)}}{\partial u_x^{(m,n)}} - \frac{\mathrm{d}}{\mathrm{d}t}\left(\frac{\partial L^{(m,n)}}{\partial \dot{u}_x^{(m,n)}}\right) = 0, \quad \frac{\partial L^{(m,n)}}{\partial u_z^{(m,n)}} - \frac{\mathrm{d}}{\mathrm{d}t}\left(\frac{\partial L^{(m,n)}}{\partial \dot{u}_z^{(m,n)}}\right) = 0, \tag{5}$$

providing the equations of motion for the inner cell:

$$\begin{aligned}
M\ddot{u}_x^{(m,n)} = {} & \tfrac{1}{2}K_{axi}^n[-4u_x^{(m,n)} + 2u_x^{(m+1,n)} + 2u_x^{(m-1,n)}] \\
& + \tfrac{1}{2}K_{dia}^n[-4u_x^{(m,n)} + u_x^{(m+1,n+1)} + u_x^{(m+1,n-1)} + u_x^{(m-1,n+1)} + u_x^{(m-1,n-1)} \\
& + u_z^{(m+1,n+1)} + u_z^{(m-1,n-1)} - u_z^{(m+1,n-1)} - u_z^{(m-1,n+1)}] \\
& + \tfrac{1}{2}K_{axi}^s[-4u_x^{(m,n)} + 2u_x^{(m,n+1)} + 2u_x^{(m,n-1)}] \\
& + \tfrac{1}{2}K_{dia}^s[-4u_x^{(m,n)} + u_x^{(m+1,n+1)} + u_x^{(m+1,n-1)} + u_x^{(m-1,n-1)} + u_x^{(m-1,n+1)} \\
& + u_z^{(m+1,n-1)} + u_z^{(m-1,n+1)} - u_z^{(m-1,n-1)} - u_z^{(m+1,n+1)}],
\end{aligned}$$

$$\begin{aligned}
M\ddot{u}_z^{(m,n)} = {} & \tfrac{1}{2}K_{axi}^n[-4u_z^{(m,n)} + 2u_z^{(m,n+1)} + 2u_z^{(m,n-1)}] \\
& + \tfrac{1}{2}K_{dia}^n[-4u_z^{(m,n)} + u_z^{(m+1,n+1)} + u_z^{(m+1,n-1)} + u_z^{(m-1,n-1)} + u_z^{(m-1,n+1)} \\
& + u_x^{(m+1,n+1)} + u_x^{(m-1,n-1)} - u_x^{(m+1,n-1)} - u_x^{(m-1,n+1)}] \\
& + \tfrac{1}{2}K_{axi}^s[-4u_z^{(m,n)} + 2u_z^{(m+1,n)} + 2u_z^{(m-1,n)}] \\
& + \tfrac{1}{2}K_{dia}^s[-4u_z^{(m,n)} + u_z^{(m+1,n+1)} + u_z^{(m+1,n-1)} + u_z^{(m-1,n+1)} + u_z^{(m-1,n-1)} \\
& + u_x^{(m+1,n-1)} + u_x^{(m-1,n+1)} - u_x^{(m+1,n+1)} - u_x^{(m-1,n-1)}],
\end{aligned} \tag{6}$$

where $\{\ddot{u}_x^{(m,n)}, \ddot{u}_z^{(m,n)}\}$ are the accelerations in x and z directions.

2.2. EQUATIONS OF MOTION FOR A BOUNDARY CELL

The procedure used for the derivation of the equations of motion for the inner cell (m, n) can also be applied to the boundary cell $(m, 0)$ depicted in Figure 3. One again starts with

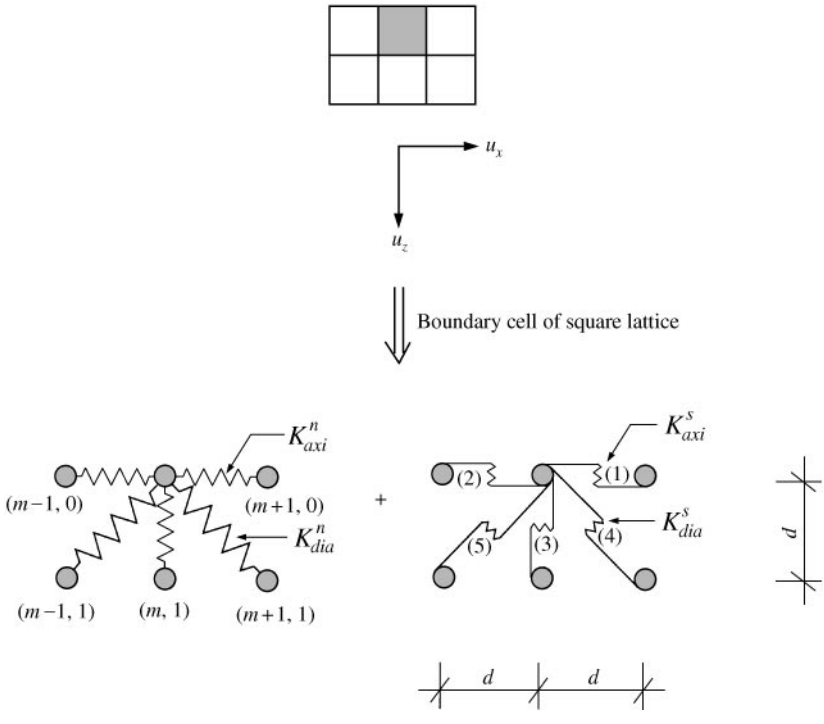

Figure 3. Boundary cell of square lattice.

presenting the potential energy, which for the boundary cell yields

$$E_{pot}^{(m,0)} = \tfrac{1}{2} \sum_{i=1}^{3} (\Delta l_{(i)}^2 K_{axi}^n + \Delta s_{(i)}^2 K_{axi}^s) + \tfrac{1}{2} \sum_{i=4}^{5} (\Delta l_{(i)}^2 K_{dia}^n + \Delta s_{(i)}^2 K_{dia}^s). \tag{7}$$

Here, the variations of spring length in the longitudinal direction $\Delta l_{(i)}$ and the shear direction $\Delta s_{(i)}$ are

$$\Delta l_{(1)} = u_x^{(m+1,0)} - u_x^{(m,0)}, \quad \Delta l_{(2)} = u_x^{(m,0)} - u_x^{(m-1,0)}, \quad \Delta l_{(3)} = u_z^{(m,1)} - u_z^{(m,0)},$$

$$\Delta l_{(4)} = \tfrac{1}{2}\sqrt{2}\,(u_x^{(m+1,1)} - u_x^{(m,0)} + u_z^{(m+1,1)} - u_z^{(m,0)}),$$

$$\Delta l_{(5)} = \tfrac{1}{2}\sqrt{2}\,(u_x^{(m,0)} - u_x^{(m-1,1)} + u_z^{(m-1,1)} - u_z^{(m,0)}),$$

$$\Delta s_{(1)} = u_z^{(m+1,0)} - u_z^{(m,0)}, \quad \Delta s_{(2)} = u_z^{(m,0)} - u_z^{(m-1,0)}, \quad \Delta s_{(3)} = u_x^{(m,0)} - u_x^{(m,1)},$$

$$\Delta s_{(4)} = \tfrac{1}{2}\sqrt{2}\,(u_x^{(m,0)} - u_x^{(m+1,1)} + u_z^{(m+1,1)} - u_z^{(m,0)}),$$

$$\Delta s_{(5)} = \tfrac{1}{2}\sqrt{2}\,(u_x^{(m,0)} - u_x^{(m-1,1)} + u_z^{(m,0)} - u_z^{(m-1,1)}). \tag{8}$$

For obvious reasons, the expression for the kinetic energy of the boundary cell has the same form as that of the inner cell (see equation (4)). By combining equations (7) and (8) with respectively, equations (1), (4) and (5), the equations of motion for the boundary cell are

obtained as

$$
\begin{aligned}
M\ddot{u}_x^{(m,0)} &= \tfrac{1}{2}K_{axi}^n[-4u_x^{(m,0)} + 2u_x^{(m+1,0)} + 2u_x^{(m-1,0)}] \\
&\quad + \tfrac{1}{2}K_{dia}^n[-2u_x^{(m,0)} + u_x^{(m+1,1)} + u_x^{(m-1,1)} + u_z^{(m+1,1)} - u_z^{(m-1,1)}] \\
&\quad + \tfrac{1}{2}K_{axi}^s[-2u_x^{(m,0)} + 2u_x^{(m,1)}] \\
&\quad + \tfrac{1}{2}K_{dia}^s[-2u_x^{(m,0)} + u_x^{(m+1,1)} + u_x^{(m-1,1)} + u_z^{(m-1,1)} - u_z^{(m+1,1)}], \\
M\ddot{u}_z^{(m,0)} &= \tfrac{1}{2}K_{axi}^n[-2u_z^{(m,0)} + 2u_z^{(m,1)}] \\
&\quad + \tfrac{1}{2}K_{dia}^n[-2u_z^{(m,0)} + u_z^{(m+1,1)} + u_z^{(m-1,1)} + u_x^{(m+1,1)} - u_x^{(m-1,1)}] \\
&\quad + \tfrac{1}{2}K_{axi}^s[-4u_z^{(m,0)} + 2u_z^{(m+1,0)} + 2u_z^{(m-1,0)}] \\
&\quad + \tfrac{1}{2}K_{dia}^s[-2u_z^{(m,0)} + u_z^{(m+1,1)} + u_z^{(m-1,1)} + u_x^{(m-1,1)} - u_x^{(m+1,1)}].
\end{aligned} \tag{9}
$$

2.3. LATTICE MODEL VERSUS CONTINUUM MODEL

In order to have a consistent relation between the macro-scale material behaviour and the micro-scale material behaviour, in the long-wave limit the equations of motion derived for the discrete lattice (6) need to reduce to the equations of motion for the classic elastic continuum [10–12, 14]. To verify this, the first step is to replace the discrete degrees of freedom of the cell (m, n) by corresponding continuous field variables,

$$
\{u_x^{(m,n)}, u_z^{(m,n)}\} = \{\tilde{u}_x, \tilde{u}_z\}\Big|_{x=md,\, z=nd}, \tag{10}
$$

in which the tilde on top of the degrees of freedom on the right-hand side denotes the continuous character. Then, the degrees of freedom of the neighbouring cells of cell (m, n), located at points $(x = (m + p)d,\ z = (n + q)d)$, are replaced by second order Taylor approximations of the continuous field variables,

$$
\begin{aligned}
\{u_x^{(m+p,n+q)}, u_z^{(m+p,n+q)}\} &\approx [\{\tilde{u}_x, \tilde{u}_z\} + pd\{\tilde{u}_{x,x}, \tilde{u}_{z,x}\} + qd\{\tilde{u}_{x,z}, \tilde{u}_{z,z}\} \\
&\quad + \tfrac{1}{2}p^2d^2\{\tilde{u}_{x,xx}, \tilde{u}_{z,xx}\} + \tfrac{1}{2}q^2d^2\{\tilde{u}_{x,zz}, \tilde{u}_{z,zz}\} + pqd^2\{\tilde{u}_{x,xz}, \tilde{u}_{z,xz}\}]\Big|_{x=md,\, z=nd},
\end{aligned} \tag{11}
$$

where x and z are spatial derivatives. Employing equations (6) and invoking equations (10) and (11) then leads to the equations of motion in the long-wave limit,

$$
\begin{aligned}
M\tilde{u}_{x,tt} &= (K_{axi}^n + K_{dia}^n + K_{dia}^s)d^2\tilde{u}_{x,xx} + 2(K_{dia}^n + K_{dia}^s)d^2\tilde{u}_{z,xz} \\
&\quad + (K_{axi}^s + K_{dia}^n + K_{dia}^s)d^2\tilde{u}_{x,zz}, \\
M\tilde{u}_{z,tt} &= (K_{axi}^n + K_{dia}^n + K_{dia}^s)d^2\tilde{u}_{z,zz} + 2(K_{dia}^n + K_{dia}^s)d^2\tilde{u}_{x,zx} \\
&\quad + (K_{axi}^s + K_{dia}^n + K_{dia}^s)d^2\tilde{u}_{z,xx},
\end{aligned} \tag{12}
$$

with t the partial derivative with respect to time. The micro-level constitutive coefficients of the lattice model can be related to macro-level constitutive coefficients by projecting

equations (12) onto the equations of motion for a classic elastic continuum,

$$\rho\tilde{u}_{x,tt} = (\lambda + 2\mu)\tilde{u}_{x,xx} + (\lambda + \mu)\tilde{u}_{z,xz} + \mu\tilde{u}_{x,zz},$$

$$\rho\tilde{u}_{z,tt} = (\lambda + 2\mu)\tilde{u}_{z,zz} + (\lambda + \mu)\tilde{u}_{x,zx} + \mu\tilde{u}_{z,xx}, \tag{13}$$

in which λ and μ are the Lamé constants and ρ is the density. Apparently, equations (12) and (13) coincide if the following equalities hold:

$$M = \rho d^3, \quad \frac{K^n_{axi} + K^n_{dia}}{d} = \lambda + 2\mu, \quad \frac{2K^n_{dia}}{d} = \lambda + \mu, \quad \frac{K^n_{dia} + K^s_{axi}}{d} = \mu, \quad K^s_{dia} = 0. \tag{14}$$

As a result of the anisotropic character of the lattice, expressions (14b) and (14c) provide two different relations for the Lamé constant λ, i.e.,

$$\lambda^{(1)} = \frac{K^n_{axi} - K^n_{dia} - 2K^s_{axi}}{d}, \quad \lambda^{(2)} = \frac{K^n_{dia} - K^s_{axi}}{d}. \tag{15}$$

For retrieving the isotropic classic elastic continuum from the long-wave approximation of the square anisotropic lattice, it is a prerequisite that equations (15a) and (15b) are equivalent, leading to the constraint

$$2K^n_{dia} = K^n_{axi} - K^s_{axi}. \tag{16}$$

Inserting expression (16) successively into equations (15) and (14c) gives for the Lamé constants λ and μ

$$\lambda = \frac{K^n_{axi} - 3K^s_{axi}}{2d}, \quad \mu = \frac{K^n_{axi} + K^s_{axi}}{2d}. \tag{17}$$

Subsequently, substituting equations (16) and (14e) into the equations of motion (6) for the inner cell (m, n) yields

$$\begin{aligned}
M\ddot{u}_x^{(m,n)} = {} & K^n_{axi}[-3u_x^{(m,n)} + u_x^{(m+1,n)} + u_x^{(m-1,n)} + \tfrac{1}{4}(u_x^{(m+1,n+1)} + u_x^{(m-1,n+1)} \\
& + u_x^{(m-1,n-1)} + u_x^{(m+1,n-1)}) + \tfrac{1}{4}(u_z^{(m+1,n+1)} + u_z^{(m-1,n-1)} \\
& - u_z^{(m+1,n-1)} - u_z^{(m-1,n+1)})] + K^s_{axi}[-u_x^{(m,n)} + u_x^{(m,n+1)} + u_x^{(m,n-1)} \\
& - \tfrac{1}{4}(u_x^{(m+1,n+1)} + u_x^{(m-1,n+1)} + u_x^{(m-1,n-1)} + u_x^{(m+1,n-1)}) \\
& - \tfrac{1}{4}(u_z^{(m+1,n+1)} + u_z^{(m-1,n-1)} - u_z^{(m+1,n-1)} - u_z^{(m-1,n+1)})], \\
M\ddot{u}_z^{(m,n)} = {} & K^n_{axi}[-3u_z^{(m,n)} + u_z^{(m,n+1)} + u_z^{(m,n-1)} + \tfrac{1}{4}(u_z^{(m+1,n+1)} + u_z^{(m+1,n-1)} \\
& + u_z^{(m-1,n-1)} + u_z^{(m-1,n+1)}) + \tfrac{1}{4}(u_x^{(m+1,n+1)} + u_x^{(m-1,n-1)} \\
& - u_x^{(m+1,n-1)} - u_x^{(m-1,n+1)})] + K^s_{axi}[-u_z^{(m,n)} + u_z^{(m+1,n)} + u_z^{(m-1,n)} \\
& - \tfrac{1}{4}(u_z^{(m+1,n+1)} + u_z^{(m+1,n-1)} + u_z^{(m-1,n-1)} + u_z^{(m-1,n+1)}) \\
& - \tfrac{1}{4}(u_x^{(m+1,n+1)} + u_x^{(m-1,n-1)} - u_x^{(m+1,n-1)} - u_x^{(m-1,n+1)})],
\end{aligned} \tag{18}$$

while substituting these constraints in the equation of motion (9) for the boundary cell $(m, 0)$ results in

$$\begin{aligned}
M\ddot{u}_x^{(m,0)} &= \tfrac{1}{2}K_{axi}^n[-5u_x^{(m,0)} + 2u_x^{(m+1,0)} + 2u_x^{(m-1,0)} + \tfrac{1}{2}u_x^{(m+1,1)} + \tfrac{1}{2}u_x^{(m-1,1)} \\
&\quad + \tfrac{1}{2}u_z^{(m+1,1)} - \tfrac{1}{2}u_z^{(m-1,1)}] + \tfrac{1}{2}K_{axi}^s[-u_x^{(m,0)} + 2u_x^{(m,1)} - \tfrac{1}{2}u_x^{(m+1,1)} \\
&\quad - \tfrac{1}{2}u_x^{(m-1,1)} - \tfrac{1}{2}u_z^{(m+1,1)} + \tfrac{1}{2}u_z^{(m-1,1)}], \\
M\ddot{u}_z^{(m,0)} &= \tfrac{1}{2}K_{axi}^n[-3u_z^{(m,0)} + 2u_z^{(m,1)} + \tfrac{1}{2}u_z^{(m+1,1)} + \tfrac{1}{2}u_z^{(m-1,1)} + \tfrac{1}{2}u_x^{(m+1,1)} \\
&\quad - \tfrac{1}{2}u_x^{(m-1,1)}] + \tfrac{1}{2}K_{axi}^s[-3u_z^{(m,0)} + 2u_z^{(m+1,0)} + 2u_z^{(m-1,0)} - \tfrac{1}{2}u_z^{(m+1,1)} \\
&\quad - \tfrac{1}{2}u_z^{(m-1,1)} - \tfrac{1}{2}u_x^{(m+1,1)} + \tfrac{1}{2}u_x^{(m-1,1)}]. \qquad (19)
\end{aligned}$$

3. DISPERSION CURVES OF BODY WAVES

Now that the equations of motion for the inner cell have been determined, the propagation of body waves through the lattice can be analyzed. To this end, a solution of equations (18) will be sought in the form of plane harmonic waves

$$\begin{aligned}
u_x^{(m,n)} &= A\exp(\mathrm{i}(\omega t - mk_x d - nk_z d)), \\
u_z^{(m,n)} &= B\exp(\mathrm{i}(\omega t - mk_x d - nk_z d)), \qquad (20)
\end{aligned}$$

in which ω is the angular frequency, A and B are the wave amplitudes and k_x and k_z are the wave numbers in the x and the z direction respectively. The vector of wave numbers $\mathbf{k} = (k_x, k_z)$ is related to the vector of wavelengths $\mathbf{\Lambda} = (\Lambda_x, \Lambda_z)$ via the scalar product

$$\mathbf{k}\cdot\mathbf{\Lambda} = 2\pi. \qquad (21)$$

Also, the vector of wave numbers is related to the vector of phase velocities $\mathbf{c} = (c_x, c_z)$ via the scalar product

$$\mathbf{k}\cdot\mathbf{c} = \omega. \qquad (22)$$

Inserting solutions (20) into the equations of motion for the inner cell (18) results in a system of homogeneous algebraic equations with respect to the wave amplitudes A and B:

$$\begin{aligned}
&A[M\omega^2 + K_{axi}^n(2\cos(k_x d) + \cos(k_x d)\cos(k_z d) - 3) + K_{axi}^s(2\cos(k_z d) \\
&\quad - \cos(k_x d)\cos(k_z d) - 1)] + B[(K_{axi}^n - K_{axi}^s)(-\sin(k_x d)\sin(k_z d))] = 0, \\
&A[(K_{axi}^n - K_{axi}^s)(-\sin(k_x d)\sin(k_z d))] + B[M\omega^2 + K_{axi}^n(2\cos(k_z d) \\
&\quad + \cos(k_x d)\cos(k_z d) - 3) + K_{axi}^s(2\cos(k_x d) - \cos(k_x d)\cos(k_z d) - 1)] = 0. \qquad (23)
\end{aligned}$$

The system of equations (23) has a non-trivial solution if, and only if, for a given set of elastic parameters, its determinant $\Delta(\omega, k_x, k_z)$ is equal to zero. This leads to

$$\begin{aligned}
&[M\omega^2 + K_{axi}^n(\cos(k_x d) + \cos(k_z d) + 2\cos(k_x d)\cos(k_z d) - 4) \\
&\quad + K_{axi}^s(\cos(k_x d) + \cos(k_z d) - 2\cos(k_x d)\cos(k_z d))] \\
&\quad \times[M\omega^2 + (K_{axi}^n + K_{axi}^s)(\cos(k_x d) + \cos(k_z d) - 2)] = 0. \qquad (24)
\end{aligned}$$

In equation (24), the first (*second*) expression between parentheses characterises the propagation of the compression wave (*shear wave*). As the lattice is anisotropic (see Figure 2), the character of the dispersion relations (24) depends on the direction of the body wave propagation. When considering the body waves to be propagating along the x-axis, an infinite number of dispersion curves can be constructed, where the individual dispersion curves are characterised by their wave number k_z in the z direction. For each body wave, the domain of dispersion curves is enclosed by a lower-frequency curve and an upper-frequency curve. The lower-frequency curve is determined by the minimum value for the normalized wave number in the z direction; $k_z d = 0$, yielding $\cos(k_z d) = 1$. The upper-frequency curve ensues upon adopting a maximum value for the normalized wave number in the z direction; $k_z d = \pi$ (or $k_z d = -\pi$), yielding $\cos(k_z d) = -1$. The backgrounds of this maximum normalized wave number will be treated in more detail later in this section.

In Figure 4, the dispersion curves for the compression wave and the shear wave are depicted. Because the dispersion curves are symmetric with respect to $k_x = 0$ and $\omega = 0$, only the positive wave number axis and the positive frequency axis have been depicted. The dispersion curves have been computed by using a Young's modulus $E = 200$ MPA, a Poisson's ratio $\nu = 0{\cdot}20$ (corresponding to Lamé constants $\lambda = 55{\cdot}5$ MPa, $\mu = 83{\cdot}3$ MPa) and a density $\rho = 1800\ \mathrm{kg/m^3}$. These parameters constitute a ballast material used in ordinary railway tracks [15]. The cell distance d of the discrete lattice relates to the diameter of the ballast particles, which has been chosen as $d = 100$ mm. This is the largest particle size that can be found in a broadly graded ballast [15]. Via the particle diameter d and the Lamé constants λ and μ, the particle contact stiffnesses K^n_{axi} and K^s_{axi} can be calculated by inverting equation (17).

The angular frequency band that will be considered for the analysis in this paper and the companion paper equals $\omega \in [0, 10\,000\ \mathrm{rad/s}]$. This approximately corresponds to a frequency band [0, 1500 Hz], whose range is reckoned to be significant for the vibrations of concrete sleepers in ballasted tracks [16–18]. Because, during an instantaneous train axle passage concrete sleepers hardly dissipate vibrations, this frequency band is expected to be transmitted almost completely to the ballast underneath.

For an increasing wave number, the sinusoidal character of the dispersion relations (24) causes a repetitiveness of zones: $k_x d \in [-\pi, \pi] + [2\pi n, 2\pi(n+1)]$, where n is an integer. These zones are commonly named "Brillouin zones", and are a typical feature in the

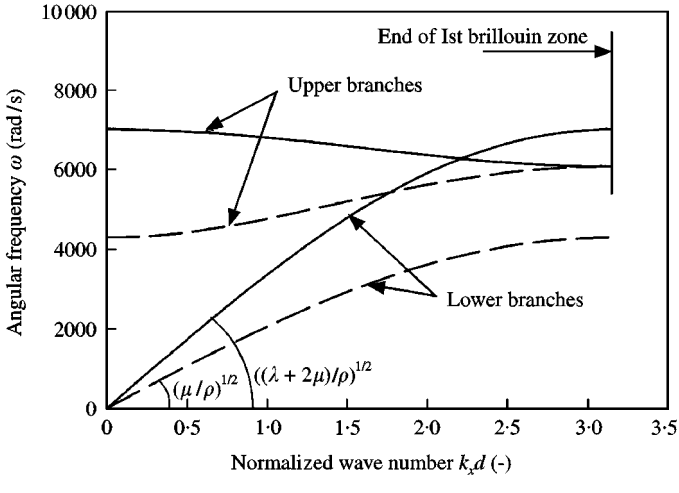

Figure 4. Body wave dispersion curves for square lattice: ——, Compression wave; – –, Shear wave.

dynamic response of a discrete system [19]. Normally, only the first Brillouin zone $k_x d \in [-\pi, \pi]$ is considered, because the incorporation of higher Brillouin zones results in a non-unique relation between the frequency and the wave number [19]. Consequently, the maximum (normalized) wave number transmitted by the discrete medium equals $k_x d = \pi$ (or $k_x d = -\pi$), relating to a minimum admissible wavelength of two times the particle diameter $\Lambda_x = 2d$. Figure 4 illustrates that at this wave number the slope of the dispersion curves is horizontal, corresponding to a *zero* group velocity: $c_x^g = \partial\omega/\partial k_x = 0$. Because for unabsorbed propagating harmonic waves the group velocity equals the velocity of the wave energy, at the maximum admissible wave number $k_x d = \pi$ the energy does not propagate. Hence, this wave can be called a *standing wave*.

As illustrated in Figure 4, at the long-wave limit $k_x d = 0$, the tangential slope of the lower-frequency curves corresponds to the body wave velocities in a classic linear elastic medium, i.e.,

$$\text{compression wave: } c_x^{compr.,k_x=0} = \sqrt{\frac{(3K_{axi}^n - K_{axi}^s)d^2}{2M}} = \sqrt{\frac{\lambda + 2\mu}{\rho}},$$

$$\text{shear wave: } c_x^{sh.,k_x=0} = \sqrt{\frac{(K_{axi}^n + K_{axi}^s)d^2}{2M}} = \sqrt{\frac{\mu}{\rho}}. \tag{25}$$

For an increasing wave number, the phase velocity of the lower-frequency curves of the discrete system starts to deviate from the corresponding continuum body wave velocity (25). This phenomenon is known as dispersion, and can be ascribed to the particle size effect, which becomes more pronounced for shorter wavelengths. The fact that the particle size is explicitly included in the discrete model, provides the dispersion curves also with a frequency maximum. Actually, the discrete medium acts as a granular filter that transmits only relatively low frequencies.

For analyzing the waves propagating through the layer, it is necessary to solve expression (24) for the wave number k_z, which, via straightforward algebra, yields the following expressions:

$$k_z^{(1),(2)} = \pm\frac{1}{d}\arccos\left(\frac{M\omega^2 + K_{axi}^n(\cos(k_x d) - 4) + K_{axi}^s\cos(k_x d)}{-K_{axi}^n(2\cos(k_x d) + 1) + K_{axi}^s(2\cos(k_x d) - 1)}\right)$$

$$k_z^{(3),(4)} = \pm\frac{1}{d}\arccos\left(\frac{-M\omega^2 - K_{axi}^n(\cos(k_x d) - 2) - K_{axi}^s(\cos(k_x d) - 2)}{K_{axi}^n + K_{axi}^s}\right). \tag{26}$$

In correspondence with the four solutions $k_z^{(j)}$, the amplitude vectors of the harmonic solutions (20) have four components as well $\mathbf{A} = [A^{(1)}, A^{(2)}, A^{(3)}, A^{(4)}]^{\mathrm{T}}$ and $\mathbf{B} = [B^{(1)}, B^{(2)}, B^{(3)}, B^{(4)}]^{\mathrm{T}}$. The eigenvector $\mathbf{D}$ that contains the amplitude ratios of the body waves $B^{(j)}/A^{(j)}$, with $j \in \{1, 2, 3, 4\}$, ensues from either equation (23a) or (23b). The former relation yields for the components of this vector

$$\begin{aligned} D^{(j)} = \frac{B^{(j)}}{A^{(j)}} = [&M\omega^2 + K_{axi}^n(2\cos(k_x d) + \cos(k_x d)\cos(k_z^{(j)} d) - 3) \\ &+ K_{axi}^s(2\cos(k_z^{(j)} d) - \cos(k_x d)\cos(k_z^{(j)} d) - 1)] \\ &\times [(K_{axi}^n - K_{axi}^s)\sin(k_x d)\sin(k_z^{(j)} d)]^{-1} \\ &\text{with } j \in \{1, 2, 3, 4\}. \end{aligned} \tag{27}$$

By combining equations (20), (26) and (27), the displacements under harmonic body wave propagation may then be formulated generally as

$$u_x^{(m,n)} = (A^{(1)}\exp(-\mathrm{i}nk_z^{(1)}d) + A^{(2)}\exp(-\mathrm{i}nk_z^{(2)}d) + A^{(3)}\exp(-\mathrm{i}nk_z^{(3)}d) + A^{(4)}\exp(-\mathrm{i}nk_z^{(4)}d))\exp(\mathrm{i}(\omega t - mk_x d)),$$

$$u_z^{(m,n)} = (A^{(1)}D^{(1)}\exp(-\mathrm{i}nk_z^{(1)}d) + A^{(2)}D^{(2)}\exp(-\mathrm{i}nk_z^{(2)}d) + A^{(3)}D^{(3)}\exp(-\mathrm{i}nk_z^{(3)}d) + A^{(4)}D^{4}\exp(-\mathrm{i}nk_z^{(4)}d))\exp(\mathrm{i}(\omega t - mk_x d)). \quad (28)$$

4. DISPERSION BRANCHES OF THE LAYER MODES

The dispersion branches that characterize the eigenmodes of the layer can be deduced by inserting the displacements under body wave propagation (28) into the boundary conditions at the top and the bottom of the layer. The eigenbehaviour of the layer is reflected by requiring the boundary cells at the top of the layer $z = 0$ to be free of loading. Accordingly, the boundary conditions at the top of the layer are equal to the equations of motion for the free boundary cell (i.e., equations (19)):

$$M\ddot{u}_x^{(m,0)} = \tfrac{1}{2}K_{axi}^n[-5u_x^{(m,0)} + 2u_x^{(m+1,0)} + 2u_x^{(m-1,0)} + \tfrac{1}{2}u_x^{(m+1,1)} + \tfrac{1}{2}u_x^{(m-1,1)} + \tfrac{1}{2}u_z^{(m+1,1)} - \tfrac{1}{2}u_z^{(m-1,1)}] + \tfrac{1}{2}K_{axi}^s[-u_x^{(m,0)} + 2u_x^{(m,1)} - \tfrac{1}{2}u_x^{(m+1,1)} - \tfrac{1}{2}u_x^{(m-1,1)} - \tfrac{1}{2}u_z^{(m+1,1)} + \tfrac{1}{2}u_z^{(m-1,1)}],$$

$$M\ddot{u}_z^{(m,0)} = \tfrac{1}{2}K_{axi}^n[-3u_z^{(m,0)} + 2u_z^{(m,1)} + \tfrac{1}{2}u_z^{(m+1,1)} + \tfrac{1}{2}u_z^{(m-1,1)} + \tfrac{1}{2}u_x^{(m+1,1)} - \tfrac{1}{2}u_x^{(m-1,1)}] + \tfrac{1}{2}K_{axi}^s[-3u_z^{(m,0)} + 2u_z^{(m+1,0)} + 2u_z^{(m-1,0)} - \tfrac{1}{2}u_z^{(m+1,1)} - \tfrac{1}{2}u_z^{(m-1,1)} - \tfrac{1}{2}u_x^{(m+1,1)} + \tfrac{1}{2}u_x^{(m-1,1)}]. \quad (29)$$

Since the bottom of the layer is assumed to be rigidly supported, the displacements at $z = nd = H$ are equal to zero:

$$u_x^{(m,H/d)} = 0, \quad u_z^{(m,H/d)} = 0. \quad (30)$$

Substitution of the expressions for body wave propagation (28) into the boundary conditions (29) and (30) provides the following set of algebraic equations:

$$[A^{(1)} + A^{(2)} + A^{(3)} + A^{(4)}][M\omega^2 + \tfrac{1}{2}K_{axi}^n(4\cos(k_x d) - 5) - \tfrac{1}{2}K_{axi}^s] + [A^{(1)}\exp(-\mathrm{i}k_z^{(1)}d) + A^{(2)}\exp(-\mathrm{i}k_z^{(2)}d) + A^{(3)}\exp(-\mathrm{i}k_z^{(3)}d) + A^{(4)}\exp(-\mathrm{i}k_z^{(4)}d)] \times [\tfrac{1}{2}K_{axi}^n\cos(k_x d) - \tfrac{1}{2}K_{axi}^s(\cos(k_x d) - 2)] + [A^{(1)}D^{(1)}\exp(-\mathrm{i}k_z^{(1)}d) + A^{(2)}D^{(2)}\exp(-\mathrm{i}k_z^{(2)}d) + A^{(3)}D^{(3)}\exp(-\mathrm{i}k_z^{(3)}d) + A^{(4)}D^{(4)}\exp(-\mathrm{i}k_z^{(4)}d)] \times [-\tfrac{1}{2}\mathrm{i}K_{axi}^n\sin(k_x d) + \tfrac{1}{2}\mathrm{i}K_{axi}^s\sin(k_x d)] = 0,$$

$$[A^{(1)}D^{(1)} + A^{(2)}D^{(2)} + A^{(3)}D^{(3)} + A^{(4)}D^{(4)}][M\omega^2 - \tfrac{3}{2}K^n_{axi} + \tfrac{1}{2}K^s_{axi}(4\cos(k_x d) - 3)]$$

$$+ [A^{(1)}D^{(1)}\exp(-\mathrm{i}k_z^{(1)}d) + A^{(2)}D^{(2)}\exp(-\mathrm{i}k_z^{(2)}d) + A^{(3)}D^{(3)}\exp(-\mathrm{i}k_z^{(3)}d)$$

$$+ A^{(4)}D^{(4)}\exp(-\mathrm{i}k_z^{(4)}d)]\,[\tfrac{1}{2}K^n_{axi}(\cos(k_x d) + 2) - \tfrac{1}{2}K^s_{axi}\cos(k_x d)]$$

$$+ [A^{(1)}\exp(-\mathrm{i}k_z^{(1)}d) + A^{(2)}\exp(-\mathrm{i}k_z^{(2)}d) + A^{(3)}\exp(-\mathrm{i}k_z^{(3)}d) + A^{(4)}\exp(-\mathrm{i}k_z^{(4)}d)]$$

$$\times[-\tfrac{1}{2}\mathrm{i}K^n_{axi}\sin(k_x d) + \tfrac{1}{2}\mathrm{i}K^s_{axi}\sin(k_x d)] = 0,$$

$$A^{(1)}\exp(-\mathrm{i}k_z^{(1)}H) + A^{(2)}\exp(-\mathrm{i}k_z^{(2)}H) + A^{(3)}\exp(-\mathrm{i}k_z^{(3)}H) + A^{(4)}\exp(-\mathrm{i}k_z^{(4)}H) = 0,$$

$$A^{(1)}D^{(1)}\exp(-\mathrm{i}k_z^{(1)}H) + A^{(2)}D^{(2)}\exp(-\mathrm{i}k_z^{(2)}H) + A^{(3)}D^{(3)}\exp(-\mathrm{i}k_z^{(3)}H)$$

$$+ A^{(4)}D^{(4)}\exp(-\mathrm{i}k_z^{(4)}H) = 0. \tag{31}$$

Here, $k_z^{(j)}$ and $D^{(j)}$ are given by equations (26) and (27) respectively. Relations (31) can be expressed in a matrix–vector format as

$$\mathbf{EA} = \mathbf{0}, \tag{32}$$

where $\mathbf{E}$ is a 4×4 matrix that governs the eigenbehaviour of the layer, and $\mathbf{A} = [A^{(1)}, A^{(2)}, A^{(3)}, A^{(4)}]^{\mathrm{T}}$ is the vector that assembles the wave amplitudes. The dispersion branches for the eigenmodes can be obtained by requiring the determinant of the matrix $\mathbf{E}$ to be equal to zero, which for a given set of elastic parameters gives

$$det\,\mathbf{E} = \Delta(\omega, k_x, H, d) = 0. \tag{33}$$

Here, the symbol Δ is used for designating the determinant. For a prescribed layer thickness H and particle diameter d, expression (33) yields a finite number of eigenmodes

$$\omega^{(j)} = \omega(k_x)^{(j)}, \quad j = 1, 2, \ldots, N, \tag{34}$$

where the total number of modes N depends on the specific choice for the particle size and the layer thickness. This will be demonstrated in a qualitative sense in sections 4.1 and 4.2.

In order to illustrate the specific features of the discrete layer modes, the dispersion branches (34) will be compared to the dispersion branches for a classic elastic continuous layer. Obviously, the dispersion branches for the continuous layer can be computed in the same manner as shown for the discrete layer. When considering the top of the continuous layer as stress-free, i.e., $\sigma_{zz} = 0$, $\sigma_{zx} = 0$, and the bottom as rigidly supported, i.e., $\tilde{u}_x = 0$, $\tilde{u}_z = 0$, similar to equations (31), a set of four characteristic equations can be deduced:

$$\tilde{A}^{(1)}(\tilde{k}_z^{(1)} + \tilde{D}^{(1)}k_x) + \tilde{A}^{(2)}(\tilde{k}_z^{(2)} + \tilde{D}^{(2)}k_x) + \tilde{A}^{(3)}(\tilde{k}_z^{(3)} + \tilde{D}^{(3)}k_x)$$

$$+ \tilde{A}^{(4)}(\tilde{k}_z^{(4)} + \tilde{D}^{(4)}k_x) = 0,$$

$$-[\tilde{A}^{(1)} + \tilde{A}^{(2)} + \tilde{A}^{(3)} + \tilde{A}^{(4)}]\mathrm{i}\lambda k_x - [\tilde{A}^{(1)}\tilde{D}^{(1)}\tilde{k}_z^{(1)} + \tilde{A}^{(2)}\tilde{D}^{(2)}\tilde{k}_z^{(2)}$$

$$+ \tilde{A}^{(3)}\tilde{D}^{(3)}\tilde{k}_z^{(3)} + \tilde{A}^{(4)}\tilde{D}^{(4)}\tilde{k}_z^{(4)}]\mathrm{i}(\lambda + 2\mu) = 0,$$

$$\tilde{A}^{(1)}\exp(-\mathrm{i}\tilde{k}_z^{(1)}H)+\tilde{A}^{(2)}\exp(-\mathrm{i}\tilde{k}_z^{(2)}H)+\tilde{A}^{(3)}\exp(-\mathrm{i}\tilde{k}_z^{(3)}H)$$
$$+\tilde{A}^{(4)}\exp(-\mathrm{i}\tilde{k}_z^{(4)}H)=0,$$
$$\tilde{A}^{(1)}\tilde{D}^{(1)}\exp(-\mathrm{i}\tilde{k}_z^{(1)}H)+\tilde{A}^{(2)}\tilde{D}^{(2)}\exp(-\mathrm{i}\tilde{k}_z^{(2)}H)+\tilde{A}^{(3)}\tilde{D}^{(3)}\exp(-\mathrm{i}\tilde{k}_z^{(3)}H)$$
$$+\tilde{A}^{(4)}\tilde{D}^{(4)}\exp(-\mathrm{i}\tilde{k}_z^{(4)}H)=0. \tag{35}$$

Here, the vector $\mathbf{A}=[\tilde{A}^{(1)},\ \tilde{A}^{(2)},\ \tilde{A}^{(3)},\ \tilde{A}^{(4)}]^{\mathrm{T}}$ assembles the wave amplitudes, with the superimposed "tilde" indicating that a continuum is concerned. Further, the four expressions for the wave number in the z direction $\tilde{k}_z^{(j)}$ are given by

$$\tilde{k}_z^{(1),(2)}=\pm\sqrt{\frac{\rho\omega^2-\mu k_x^2}{\mu}},\quad \tilde{k}_z^{(3),(4)}=\pm\sqrt{\frac{\rho\omega^2-(\lambda+2\mu)k_x^2}{\lambda+2\mu}}, \tag{36}$$

while the amplitude ratios $\tilde{D}^{(j)}$ are

$$\tilde{D}^{(j)}=\frac{\tilde{B}^{(j)}}{\tilde{A}^{(j)}}=\frac{\rho\omega^2-(\lambda+2\mu)k_x^2-\mu(\tilde{k}_z^{(j)})^2}{(\lambda+\mu)k_x\tilde{k}_z^{(j)}}\quad\text{with } j\in\{1,\,2,\,3,\,4\}. \tag{37}$$

In correspondence with equations (36) and (37), the body wave propagation through the continuum is expressed as

$$\tilde{u}_x=[\tilde{A}^{(1)}\exp(-\mathrm{i}\tilde{k}_z^{(1)}z)+\tilde{A}^{(2)}\exp(-\mathrm{i}\tilde{k}_z^{(2)}z)+\tilde{A}^{(3)}\exp(-\mathrm{i}\tilde{k}_z^{(3)}z)$$
$$+\tilde{A}^{(4)}\exp(-\mathrm{i}\tilde{k}_z^{(4)}z)]\exp(\mathrm{i}(\omega t-k_x x)),$$
$$\tilde{u}_z=[\tilde{A}^{(1)}\tilde{D}^{(1)}\exp(-\mathrm{i}\tilde{k}_z^{(1)}z)+\tilde{A}^{(2)}\tilde{D}^{(2)}\exp(-\mathrm{i}\tilde{k}_z^{(2)}z)+\tilde{A}^{(3)}\tilde{D}^{(3)}\exp(-\mathrm{i}\tilde{k}_z^{(3)}z)$$
$$+\tilde{A}^{(4)}\tilde{D}^{(4)}\exp(-\mathrm{i}\tilde{k}_z^{(4)}z)]\exp(\mathrm{i}(\omega t-k_x x)), \tag{38}$$

which resembles equations (28) for the discrete model. Due to the complex character of equations (31) and (35), the dispersion curves for the discrete layer and the continuous layer can be derived only numerically. This will be done for various parameter combinations.

4.1. VARIATION OF PARTICLE SIZE

Figure 5 shows the dispersion curves for the four lowest eigenmodes of the discrete layer (solid lines) and the continuous layer (dashed lines). The dispersion branches for a continuous layer have been previously discussed by other authors (see, for example, references [7, 20, 21]), though in these contributions, instead of using the actual displacements, displacement potentials were employed. The particle radius in the discrete model has been chosen relatively small, $r=0{\cdot}5\ \mathrm{d}=1$ mm, while the layer thickness is assumed as $H=300$ mm. The elasticity parameters and the material density correspond to the values introduced in section 3, i.e., $E=200$ MPa, $\nu=0{\cdot}20$, $\rho=1800\ \mathrm{kg/m^3}$. Due to symmetry with respect to $k_x=0$ and $\omega=0$, only the positive wave number axis and positive frequency axis have been depicted.

Due to the small particle size, in the domain considered the dispersion curves of the discrete layer and the continuous layer closely agree. Apparently, for both the discrete layer and the continuous layer it looks as if the individual dispersion curves locally intersect. However, because the eigenmodes of the layer are coupled, the individual dispersion curves may approach each other very closely, but there will never be any contact.

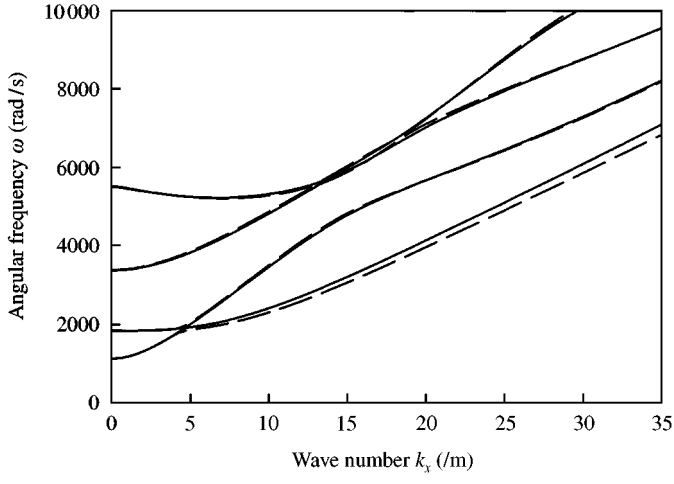

Figure 5. Dispersion branches for the four lowest eigenmodes of the discrete layer (——, $r = 1$ mm, $H = 300$ mm) and the continuous layer (- - - - -, $H = 300$ mm).

For the continuous layer, the total number of eigenmodes is infinite. This is different for the discrete layer, which has a finite number of eigenmodes as a result of the frequency filtering by the discrete particles. The highest layer mode possible approaches the upper-frequency curve of the compression body wave. In fact, in the frequency range where body waves cannot be transmitted, layer modes also cannot emerge. Although in Figure (5) only the four lowest modes are depicted, actually a very large number of layer modes exists. This is, since for a relatively small particle radius of $r = 1$ mm, the bounding behaviour by the upper frequency curves for the body waves occurs in the very high-frequency range. However, by increasing the particle size to $r = 50$ mm, the upper-frequency curves for the body waves considerably descend along the frequency axis, causing the total number of modes to be reduced to only six modes. This is shown in Figure 6, in which the layer dispersion curves have been plotted together with the body wave dispersion curves. Here, the characteristic limitation of the layer modes by the envelope of the high-frequency body wave curves is clearly illustrated. It can also be noticed that at the end of the first Brillouin zone, $k_x d = \pi$, all dispersion curves show a horizontal tangential slope. The zero group velocity at this stage implies that no wave energy is conveyed anymore, so that the modes degenerate into a standing wave.

As for the body wave dispersion curves, the dispersion curves for the eigenmodes of the layer are periodic with respect to the Brillouin zones, i.e.,

$$\omega(k_x)^{(j)} = \omega(k_x + 2\pi n/d)^{(j)}, \quad \text{where } n \in Z, \tag{39}$$

with j the mode number and n an arbitrary integer. For reasons mentioned previously, the eigenmodes have no clear physical meaning for wave lengths smaller than two times the particle diameter. In Figure 6, this minimum admissible wavelength is reflected by a maximum admissible wave number $k_x^{max} = \pi/d \approx 31{\cdot}4$/m, which thus borders the first Brillouin zone.

4.2. VARIATION OF LAYER THICKNESS

For investigating how the characteristics of the layer modes are influenced by the layer thickness, the layer thickness is increased from 300 to 600 mm while keeping the particle

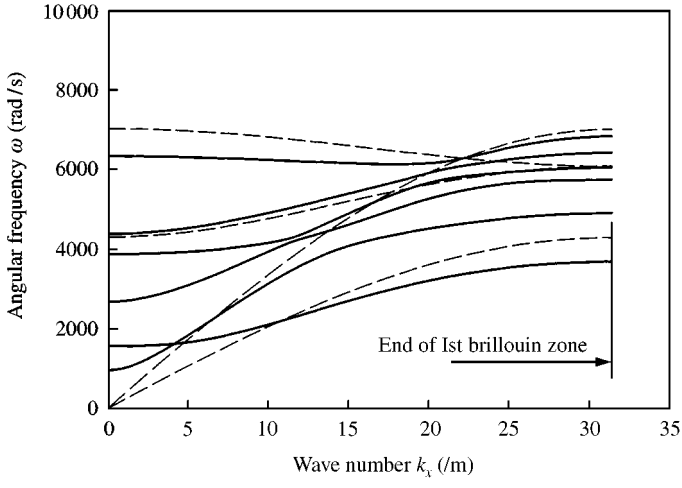

Figure 6. Dispersion branches for the eigenmodes (——) and the body waves (- - - - -) of the discrete layer ($r = 50$ mm, $H = 300$ mm).

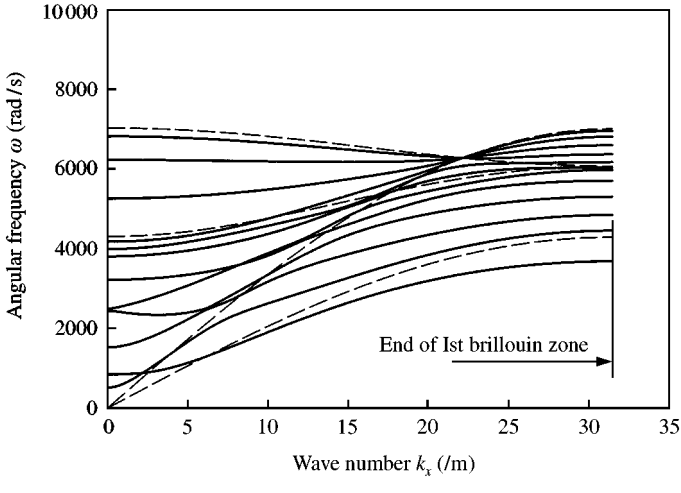

Figure 7. Dispersion branches for the eigenmodes (——) and the body waves (- - - - -) of the discrete layer ($r = 50$ mm, $H = 600$ mm).

radius constant, $r = 50$ mm. Figure 7 shows that the total number of layer modes then increases from 6 to 12. The reason for the increasing number of layer modes is that a thicker layer reduces the frequencies of the modes, thereby causing more modes to be captured in the domain bordered by the envelope of the high-frequency body wave curves.

The current parameter study has demonstrated that the magnitude of the minimum admissible wavelength depends only on the size of the particles. On the other hand, the total number of layer modes is determined by both the particle size and the layer thickness. Because there are two length-scale parameters involved in the layer model, it is not possible to normalize the dispersion curves for arbitrary length-scale parameters into one unique graphical representation, as often is done for a continuous layer that contains only one length-scale parameter (see, for example, reference [20]).

5. CONCLUSION

In this paper, the harmonic body wave propagation as well as the eigenmodes for a layer of discrete particles have been analyzed. The discrete character of the layer has been modelled by a square lattice, consisting of individual cells that are connected by longitudinal springs and shear springs. After deriving the equations of motion for a lattice cell, the propagation characteristics of the harmonic body waves have been elaborated. It has been demonstrated that the dispersive behaviour of the body waves becomes more pronounced for shorter wavelengths, as a result of the discrete nature of the layer. The particles thereby cause the higher frequencies to be retained. This feature does not appear during wave propagation through a continuous medium.

It has been shown that a discrete layer has a limited number of eigenmodes. This number is determined by the size of the particles in combination with the thickness of the layer. More specifically, a larger (*smaller*) particle size decreases (*increases*) the number of eigenmodes, while a larger (*smaller*) layer thickness increases (*decreases*) the number of eigenmodes. Further, for smaller particles the dispersion curves for the discrete layer approach the dispersion curves for a continuous layer more closely.

In the companion paper, the response of the discrete layer to a moving, harmonically vibrating load will be investigated. This analysis reflects the dynamic behaviour of a layer of ballast particles subjected to an instantaneous train axle passage.

REFERENCES

1. H. A. Dieterman and A. Metrikine 1996 *European Journal of Mechanics A/Solids* **15**, 67–90. The equivalent stiffness of a half space interacting with a beam. Critical velocities of a moving load along the beam.
2. A. S. J. Suiker, R. De Borst and C. Esveld 1998 *Archives of Applied Mechanics* **68**, 158–168. Critical behaviour of a Timoshenko beam-half plane system under a moving load.
3. G. A. Hunt 1994 *Technical Report LR TM* 031, *British Rail Research, London, England*. Analysis of requirements for railway construction on soft ground.
4. J-P. Fortin 1982 *Revue Générale de Chemins de Fer* **101**, 93–102. La déformée dynamique de la voie ferrée.
5. J. J. Labra 1975 *Acta Mechanica* **22**, 113–129. An axially stressed railroad track on an elastic continuum subjected to a moving load.
6. L. J. Fryba 1972 *Vibration of Solids and Structures under Moving Loads*. Noordhoff International Publishing, Groningen.
7. H. A. Dieterman and A. Metrikine 1997 *Journal of Applied Mechanics ASME* **64**, 596–600. Critical velocities of a harmonic load moving uniformly along an elastic layer.
8. A. S. J. Suiker, C. S. Chang, R. De Borst and C. Esveld 1999 *European Journal of Mechanics A/Solids* **18**, 749–768. Surface waves in a stratified half space with enhanced continuum properties — part 1—Formulation of the boundary value problem.
9. A. S. J. Suiker, C. S. Chang, R. De Borst and C. Esveld 1999 *European Journal of Mechanics A/Solids* **18**, 769–784. Surface waves in a stratified half space with enhanced continuum properties — part 2—Analysis of the wave characteristics in regard to high-speed railway tracks.
10. M. Born and K. Huang 1954 *Dynamical Theory of Crystal Lattices*. Oxford: Clarendon Press.
11. I. A. Kunin 1983 *Elastic Media with Microstructure, Vol. 2, Three-Dimensional Models*. Berlin: Springer.
12. A. S. J. Suiker, A. V. Metrikine and R. De Borst 2000 *International Journal of Solids and Structures* (in press). Comparison of wave propagation characteristics of the Cosserat continuum model and corresponding discrete lattice models.
13. L. D. Landau and E. M. Lifshitz 1976 *Mechanics*. Oxford: Pergamon.
14. A. A. Maradudin, E. M. Montroll, G. H. Weiss and I. P. Ipatova 1971 *Theory of Lattice Dynamics in the Harmonic Approximation*, Solid State Physics, Suppl. 3, New York: Academic.
15. E. T. Selig and J. M. Waters 1994 *Track Geotechnology and Substructure Management*. London: Thomas Telford Services Ltd.

16. K. KNOTHE and S. L. GRASSIE 1993 *Vehicle System Dynamics* **22**, 209–262. Modelling of railway track and of vehicle/track interaction at high frequencies.
17. S. L. GRASSIE 1995 *Journal of Sound and Vibration* **187**, 799–813. Dynamic modelling of concrete railway sleepers.
18. A. NORDBORG 1998 *Acta Acustica* **84**, 280–288. Vertical rail vibrations: pointforce excitation.
19. L. BRILLOUIN 1946 *Wave Propagation in Periodic Structures*. New York: Dover Publications.
20. M. E. EWING, W. S. JARDETZKY and F. PRESS 1957 *Elastic Waves in Layered Media*. New York: McGraw-Hill.
21. J. D. ACHENBACH 1973 *Wave Propagation in Elastic Solids*. Amsterdam: Elsevier Science.